



Hierarchical Ni₂P@Ni(OH)₂ architectures supported on carbon cloth as battery-type electrodes for hybrid supercapacitors with boosting specific capacitance and cycle stability

Yingying Lan^{1,2}, Hongna Xing¹, Yan Zong¹, Yong Sun¹, Linxue Zhang^{1,3}, Yajing Wang¹, Xinghua Li¹, and Xinliang Zheng^{1,*}

¹ School of Physics, Northwest University, Xi'an 710127, Shaanxi, China

² Songshan Lake Materials Laboratory, Dongguan 523808, Guangdong, China

³ School of Medical Engineering and Technology, Xinjiang Medical University, Urumqi 830011, Xinjiang, China

Received: 11 December 2020

Accepted: 8 February 2021

Published online:

1 March 2021

© The Author(s), under exclusive licence to Springer Science+Business Media, LLC part of Springer Nature 2021

ABSTRACT

In this work, a novel binder-free electrode, in which three-dimensional porous Ni₂P@Ni(OH)₂ nanosheet arrays were in situ grown on carbon cloth (CC), is rationally designed for supercapacitor applications. In comparison with Ni₂P@CC, the Ni₂P@Ni(OH)₂@CC electrode represents superior electrochemical characteristics: the gravimetric capacitance and areal capacitance are boosted to be 632 C g⁻¹ and 0.73 C cm⁻² at 1 mA cm⁻², about 2 and 2.7 times larger than those of Ni₂P@CC (321 C g⁻¹ and 0.27 C cm⁻²), respectively; the rate capability is improved to be 63.3% from 1 to 10 mA cm⁻², about 1.5 times larger than Ni₂P@CC (42.9%); the cycle stability is enhanced to be 81.4% after 1000 cycles, about 1.6 times larger than Ni₂P/CC (51.8%). The assembly Ni₂P@Ni(OH)₂@CC//AC hybrid supercapacitor device shows high energy density of 23.5 Wh kg⁻¹ at a power density of 1158.0 W kg⁻¹ and good cycling stability of 75.2% maintenance after 5000 cycles. Benefiting from the combined advantages of high electronic conductivity and large specific capacitance of Ni₂P, superior anion exchanging/intercalating capacity of Ni(OH)₂, excellent flexibility of carbon cloth, and special hierarchical architecture with large surface area, the Ni₂P@Ni(OH)₂@CC electrode is promised to be a good candidate for supercapacitors.

Yingying Lan and Hongna Xing have contributed equally to this work.

Address correspondence to E-mail: zhengxl@nwu.edu.cn

<https://doi.org/10.1007/s10854-021-05521-5>

1 Introduction

As the depletion of non-renewable fossil fuels and consequent environmental pollutions are ever-increasing serious, the exploration of clean and renewable energy sources, such as solar, wind, tide, and geothermal, has drawn growing concerns [1–4]. However, these energy sources are shackled by time or region, and the utilization efficiency is relatively low [5–7]. Developing novel high-efficient energy storage and conversion systems are urgently demanded. Supercapacitors has attracted widespread attention, owing to their specific features, such as higher power density than batteries, larger specific energy than conventional capacitors, reliable cycling stability, fast charge/discharge rates, safety, low cost, and environmental friendliness [8–11]. However, the low energy density of supercapacitors limits its practical application [12–14]. According to the energy storage mechanism, supercapacitors can be divided into two types: electrical double-layer capacitors (EDLCs) and pseudocapacitors (PCs) [15–18]. Generally, PCs possess larger energy storage ability than EDLCs, due to that the electrode materials of PCs show rich oxidation states for faradaic redox reactions. The core technology of PCs is exploring novel electrode materials with high specific capacitance.

Recently, battery-type electrode materials, especially transition metal compounds, have been widely used for supercapacitors. This is owing to their efficient faradaic redox reactions [19–21]. As a kind of n-type semiconductors, metal phosphides have two types of bonding states: the covalent bonded metal cations can store charges through faradaic redox reactions; the metal bonded atoms can improve the electrical conductivity through free electrons [22]. This specific structure makes metal phosphides possess metalloid property and excellent electrical conductivity. Compared with oxygen atom, phosphorus atom in metal phosphides is more electronegative, which can result in faster electron migration and superior redox activity [23]. These features are beneficial for electron transport that can improve the rate capability [24]. The transition metal phosphides (TMPs) have larger theoretical capacitance and higher electrical conductivity in comparison with the transition metal oxides (TMOs) [25]. Moreover, the nanostructures of TMPs are usually highly tunable for the access of electrolytes, leading to excellent

intra- and inter-particle conductivity, which is also important for electrode materials [26]. These intrinsic chemical/physical features make TMPs potential for supercapacitors. Wang et al. prepared amorphous Ni–P nanomaterials by a solvothermal route, which show a large specific capacitance of 1595 F g^{-1} at 0.5 A g^{-1} and 71.4% capacitance preserved after 1000 cycles [27]. Lu et al. fabricated spherical- and rod-like Ni_2P nanostructures by hydrothermal phosphidation two-step process, and found that the rod-like Ni_2P nanostructures have a larger specific capacitance of 799.2 F g^{-1} at 1 A g^{-1} and cycling stability of 68.4% after 2500 cycles [28]. Obviously, the metal phosphides present remarkable electrochemical performance, but their specific capacitance and cycle stability still need to be further improved.

Generally, interface construction can introduce interfacial charge migration owing to the generated strain at the interface, which is promised to be an effective way to boost the electrochemical properties of electrode materials [29, 30]. Hierarchical core–shell architectures are proposed to be a kind of hybrid nanostructures that can enlarge the surface/interface area, improve the contact of electrode/electrolyte, and shorten the channel of ion diffusion [31–33]. Especially, properly constructing core–shell architectures composed of core with large electrical conductivity and shell with pseudocapacitance are promised to be of great significance for supercapacitors [34, 35]. The particular heterostructure may induce internal electric fields and discontinuous charges at the interface, which can enhance the electric/ionic conductivity and improve the redox reaction kinetics. Besides, this core–shell heterostructure can enhance the electron storage/delivery pathway, facilitate the redox reactions, and improve the durability. Metal layered double hydroxides (LDHs) with hydrotalcite-like structure and pseudocapacitance have drawn many attentions as supercapacitors, due to their excellent anion exchanging capability and remarkable intercalating ability [36–38]. Therefore, appropriately integrating metal phosphides with hydroxides is promised to be a superior electrode material for supercapacitors, which is expected to enhance the capacitance and improve the cycle stability.

Inspired by the aspects mentioned above, we fabricated hierarchical $\text{Ni}_2\text{P}@ \text{Ni}(\text{OH})_2$ architecture grown on carbon cloth (CC) through a combined phosphorization and hydrothermal route. The

$\text{Ni}_2\text{P@Ni(OH)}_2\text{@CC}$ is directly used as a binder-free battery-type electrode for hybrid supercapacitors. In addition to the synergistic effects of combined advantages for Ni_2P and Ni(OH)_2 as mentioned above, the $\text{Ni}_2\text{P@Ni(OH)}_2\text{@CC}$ electrode is also promised to possess multiple advantages. First, the $\text{Ni}_2\text{P@Ni(OH)}_2$ composites show three-dimensional hierarchical architectures, in which both the Ni_2P and Ni(OH)_2 components show ultrathin nanosheet structures. The special hierarchical structure is supposed to have large surface area and rich electroactive sites, which make the contact between electrode materials and electrolyte more sufficient. Second, as a cheap conductive textile, carbon cloth is used as flexible substrate and current collector, which possesses desirable features, such as low cost, chemical stability, high conductivity, and excellent mechanical flexibility. Third, hierarchical $\text{Ni}_2\text{P@Ni(OH)}_2$ architectures were directly grown on the flexible conductive carbon cloth substrate without using organic binders, which can reduce the resistance between electrode materials and substrate, promoting the charge transfer. These benefits make the $\text{Ni}_2\text{P@Ni(OH)}_2\text{@CC}$ electrode a promised candidate for supercapacitors.

2 Experiment details

2.1 Reagents

$\text{NiCl}_2 \cdot 6\text{H}_2\text{O}$ was obtained from Tianjin Guangfu Fine Chemical Industry Research Institute. Tetramethylamine (HMT), $\text{NaH}_2\text{PO}_2 \cdot \text{H}_2\text{O}$, and potassium hydroxide (KOH) were purchased from Sinopharm Chemical Reagents Co., Ltd., China. Before experiment, the carbon cloth (CC) with a size of $1\text{ cm} \times 2\text{ cm}$ was successively cleaned by ultrasonication in ethanol and deionized water for each 30 min, and finally dried at $60\text{ }^\circ\text{C}$ for 8 h under vacuum conditions.

2.2 Synthesis of hierarchical Ni(OH)_2 nanoarray precursor on CC

Ni(OH)_2 nanosheet arrays were directly grown on CC by a simple hydrothermal route. $\text{NiCl}_2 \cdot 6\text{H}_2\text{O}$ (4 mmol) and HMT (1.6 g) were dissolved into deionized water (60 ml) under magnetic stirring. Then, the above solution was poured into a Teflon-lined

stainless-steel autoclave (100 mL), and several pieces of CC were immersed into the above solution. The autoclave was sealed and then heated at $100\text{ }^\circ\text{C}$ for 6 h in an electric oven. After the reaction was finished, the $\text{Ni(OH)}_2\text{@CC}$ electrode was rinsed with deionized water and ethanol, and dried at $60\text{ }^\circ\text{C}$.

2.3 Synthesis of hierarchical $\text{Ni}_2\text{P@CC}$

$\text{Ni}_2\text{P@CC}$ was fabricated by phosphorization route using $\text{Ni(OH)}_2\text{@CC}$ as precursor. Typically, the prepared $\text{Ni(OH)}_2\text{@CC}$ and $\text{NaH}_2\text{PO}_2 \cdot \text{H}_2\text{O}$ were put at two separated positions in a quartz boat with $\text{NaH}_2\text{PO}_2 \cdot \text{H}_2\text{O}$ at the upstream side of the tube furnace. The tube furnace was heated to $300\text{ }^\circ\text{C}$ with a heating rate of $2\text{ }^\circ\text{C}/\text{min}$ and kept at $300\text{ }^\circ\text{C}$ for 2 h. During all the processes, the furnace was protected in Ar atmosphere.

2.4 Synthesis of $\text{Ni}_2\text{P@Ni(OH)}_2\text{@CC}$

$\text{Ni}_2\text{P@Ni(OH)}_2\text{@CC}$ was fabricated by a second hydrothermal route. The detailed processes were consistent with the preparation method of $\text{Ni(OH)}_2\text{@CC}$ precursor. $\text{Ni}_2\text{P@CC}$ was immersed into the solution instead of CC, which was used as the substrate. Besides, the autoclave was kept at $100\text{ }^\circ\text{C}$ for 90 min.

2.5 Characterization

The structures of samples were determined by X-ray diffraction (XRD) using Cu K_α radiation (DX-2700, $\lambda = 1.5418\text{ \AA}$) in the 2θ range of 10° – 80° with a step size of 0.02° . The morphologies were characterized by scanning electron microscopy (FESEM, Hitachi S-4800 microscope) and transmission electron microscopy TEM (FEI Tecnai $\text{G}^2\text{ F20}$). The elemental compositions were tested by X-ray photoelectron spectroscopy (XPS, ESCALAB210) and Energy-dispersive spectroscopy (EDS) equipped in SEM. The Ni contents of active material were determined by inductively coupled plasma emission spectrometer (ICP-MS, 720-ES, VARIAN).

2.6 Electrochemical measurements

Electrochemical analyses were performed on a CHI 760E electrochemical workstation (Shanghai CH Instrument Company). Cyclic voltammetry (CV),

galvanostatic charge–discharge (GCD), and electrochemical impedance spectroscopy (EIS) of the samples were carried out in a three-electrode setup using 6 M KOH aqueous solution as the electrolyte. The fabricated electrodes, standard calomel electrode (SCE), and Pt electrode were used as working electrode, reference electrode, and counter electrode, respectively.

The specific capacitance is calculated from the GCD curves according to the following equations [39, 40]:

$$C_m = I\Delta t/m, \quad (1)$$

$$C_s = I\Delta t/s, \quad (2)$$

where C_m is the gravimetric capacitance ($C\ g^{-1}$), C_s is the areal capacitance ($C\ cm^{-2}$), I is the discharge current (A), Δt represents the discharging time (s), and m and s designate the mass of active material (g) and geometrical area (cm^2), respectively.

2.7 Assembly of the hybrid supercapacitor device

The hybrid supercapacitor (HSC) was assembled using $Ni_2P@Ni(OH)_2@CC$ as the positive electrode and active carbon as the negative electrode. The HSC was packaged in a 2032-type button cell, in which a polypropylene membrane was used to separate the two electrodes. The negative electrode was fabricated by mixing activated carbon (AC), acetylene black, and polytetrafluoroethylene (PTFE) with a weight ratio of 8:1:1. The forming slurry was painted on CC substrate and then dried at $60\ ^\circ C$ in a vacuum oven for 12 h. Generally, the positive and negative electrodes in the HSC device should satisfy charge balance principle ($q^+ = q^-$). The mass of AC can be obtained by the following equations [21]:

$$q = C_m \times m \times \Delta V, \quad (3)$$

$$\frac{m_+}{m_-} = \frac{C_m^- \times \Delta V^-}{C_m^+ \times \Delta V^+}, \quad (4)$$

where m is the weight of active material, C_m is the specific capacity and ΔV is the potential window of electrode. The superscripts of “+” and “-” present the positive and negative electrodes, respectively.

The energy density (E) and power density (P) can be calculated by the following equations [41]:

$$E = I \int V(t)dt/m, \quad (5)$$

$$P = E/\Delta t. \quad (6)$$

3 Results and discussions

Figure 1 shows the possible formation mechanism of hierarchical $Ni_2P@Ni(OH)_2@CC$ electrode. Firstly, the hierarchical $Ni(OH)_2$ nanoarray precursor was in situ grown on flexible carbon cloth (CC) at a low temperature of $100\ ^\circ C$ through a facile hydrothermal method. Then, the $Ni(OH)_2@CC$ precursor was treated at $300\ ^\circ C$ by a phosphorization route using $NaH_2PO_2 \cdot H_2O$ as the phosphorus source, forming $Ni_2P@CC$. Finally, $Ni_2P@CC$ was treated by a secondary hydrothermal route, resulting in the formation of $Ni_2P@Ni(OH)_2@CC$ electrode. Fig. S1a shows the XRD pattern of $Ni_2P@Ni(OH)_2@CC$. Only the diffraction peaks of Ni_2P (JCPDS: 74–1385) are obtained. The additional diffraction peak at about 26° belongs to carbon (JCPDS: 38-0715) from the CC substrate. No diffraction peaks of $Ni(OH)_2$ are found. This is mainly due to the combined effects of low crystallinity of hydroxides and tiny amount of $Ni(OH)_2$ on the CC substrate (the mass loadings of Ni_2P and $Ni_2P@Ni(OH)_2$ on CC substrate are 0.85 and

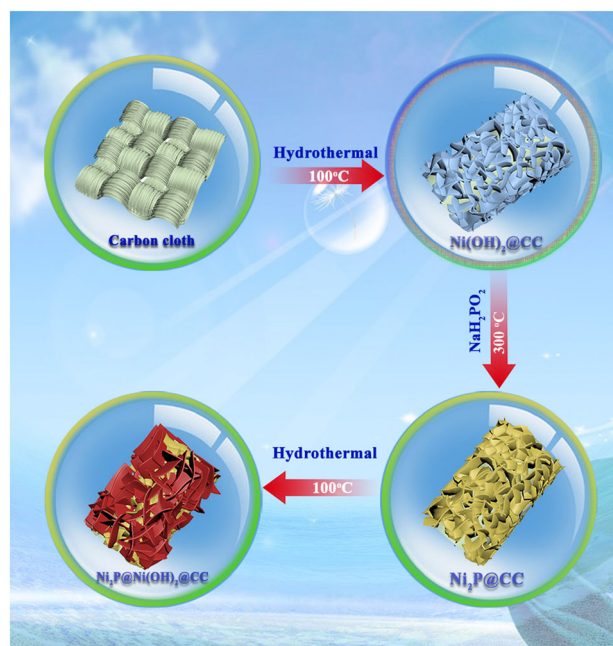


Fig. 1 Schematic illustration for the formation mechanism of flexible hierarchical $Ni_2P@Ni(OH)_2@CC$ electrode

1.15 mg cm⁻², respectively). To further examine the crystalline phases of active materials in the electrodes, the corresponding nanopowders which were fabricated by the same process are also analyzed by XRD technology, as shown in Fig. S1b. The diffraction peaks of precursor (red line) can be well indexed into α -Ni(OH)₂ with layered hydroxide structure. The broad diffraction peaks suggest that the α -Ni(OH)₂ component has a low crystallinity. After phosphorization treatment, the diffraction peaks (black line) can be assigned to Ni₂P with hexagonal phase. The XRD patterns of nanopowders further demonstrate the success of phosphorization treatment.

Figure 2a shows the optical photographs of CC substrate, Ni(OH)₂@CC, Ni₂P@CC, and Ni₂P@Ni(OH)₂@CC. Obviously, the color of the slices changes after each preparation process, suggesting that the active materials were successfully in situ grown on the CC substrate as we desired. Optical photograph presented in Fig. 2b shows that the Ni₂P@Ni(OH)₂@CC electrode is flexible, which is of great significance for the practical applications of supercapacitors. The morphologies and microstructures of the electrodes were characterized by SEM and TEM. The CC substrate is weaved by crossed carbon microfibers (Fig. S2). After in situ growth, the active materials with high density are densely packed on the microfibers of CC substrate (Figs. 2c and S2b, c). From the high-magnification SEM image (Inset of Fig. 2c), the Ni₂P@Ni(OH)₂ shows a three-dimensional (3D) hierarchical architecture which is assembled by uninterrupted ultrathin nanosheets. The interconnected nanosheets of Ni₂P and Ni(OH)₂ result in the formation of 3D network structure with multi-porous surface, which is promised to provide high specific surface area and abundant open space. This unique structure can provide numerous electroactive sites and fast ionic diffusion pathway, which are beneficial for their electrochemical behaviors. EDS spectrum of Ni₂P@Ni(OH)₂@CC (Fig. S3) contains C, O, P, and Ni elements, which is consistent with the XRD results. The EDS elemental mappings of Ni₂P@Ni(OH)₂@CC (Fig. 2d) further confirm that the Ni, P, and O elements are uniformly distributed throughout the whole CC microfiber. Compared to the mapping of P element, the mappings of Ni and O elements show relatively larger distribution areas, suggesting that Ni(OH)₂ nanosheets successfully cover on the surface of Ni₂P after the second hydrothermal route. ICP data (Table S1) reveals that

the ratio of Ni and P in Ni₂P@Ni(OH)₂@CC is greater than 2:1, further confirming that the desired phase has been successfully formed. For TEM characterization, the active materials were scraped off from the CC substrate. Figure 2e, f shows the representative TEM images of Ni₂P@Ni(OH)₂. HRTEM image in Fig. 2f shows interplanar spacing distances of 0.204 and 0.233 nm, corresponding to the (201) crystalline plane of Ni₂P and (015) crystalline plane of Ni(OH)₂, respectively.

The surface chemical constitutions and electronic states of Ni₂P@CC and Ni₂P@Ni(OH)₂@CC electrodes were characterized by XPS. Full-scan XPS spectrum of Ni₂P@Ni(OH)₂@CC (Fig. S4) indicates the existence of C, O, Ni, and P elements in the electrodes. Figure 3a shows the high-resolution Ni 2p XPS spectra of Ni₂P@CC and Ni₂P@Ni(OH)₂@CC electrodes. For the Ni₂P@CC (the down line in Fig. 3a), the spectrum shows two spin-orbit doublets peaks at 857.6 and 875.2 eV, corresponding to the Ni 2p_{3/2} and Ni 2p_{1/2} of Ni²⁺, respectively. Besides, two obvious shakeup peaks at 862.5 and 880.6 eV are related to the Ni 2p_{3/2} satellite and Ni 2p_{1/2} satellite, respectively. The peaks at 853.0 eV is probably attributed to the metallic Ni with binding energy of 852.6 eV, which is due to the partially charged Ni species (Ni^{δ+}, δ is closed to 0) [42]. The high-resolution XPS spectrum of Ni 2p of Ni₂P@Ni(OH)₂@CC (top line in Fig. 3a) consists of two spin-orbit doublets characteristics accompanied by two shakeup satellites. The doublet fitting peaks with binding energies at 857.1 and 874.8 eV correspond to the Ni 2p_{3/2} and Ni 2p_{1/2} of Ni²⁺, respectively. The other two peaks are two plump shake-up satellite peaks (denoted as “Sat.”) of Ni²⁺ [43]. Compared to Ni₂P@CC, the Ni 2p_{3/2} peak of Ni₂P@Ni(OH)₂@CC shifts to lower binding energy with a difference of 0.5 eV. High-resolution P 2p XPS spectra (Fig. 3b) show that the P 2p peaks in Ni₂P@CC and Ni₂P@Ni(OH)₂@CC are 134.7 and 133.6 eV, respectively, corresponding to the typical of phosphate species, which is mainly due to the partial superficial passivation of P species [44]. Obviously, the P 2p peak in Ni₂P@Ni(OH)₂@CC also shifts to lower binding energy with a big difference of 1.1 eV, which is probably due to the improved electron cloud density around the P atoms by the introduction of Ni(OH)₂. These obvious shift phenomena of Ni 2p and P 2p indicate the possible existence of strong electronic interactions and electron transfer at the interface between Ni₂P and Ni(OH)₂ [45]. The

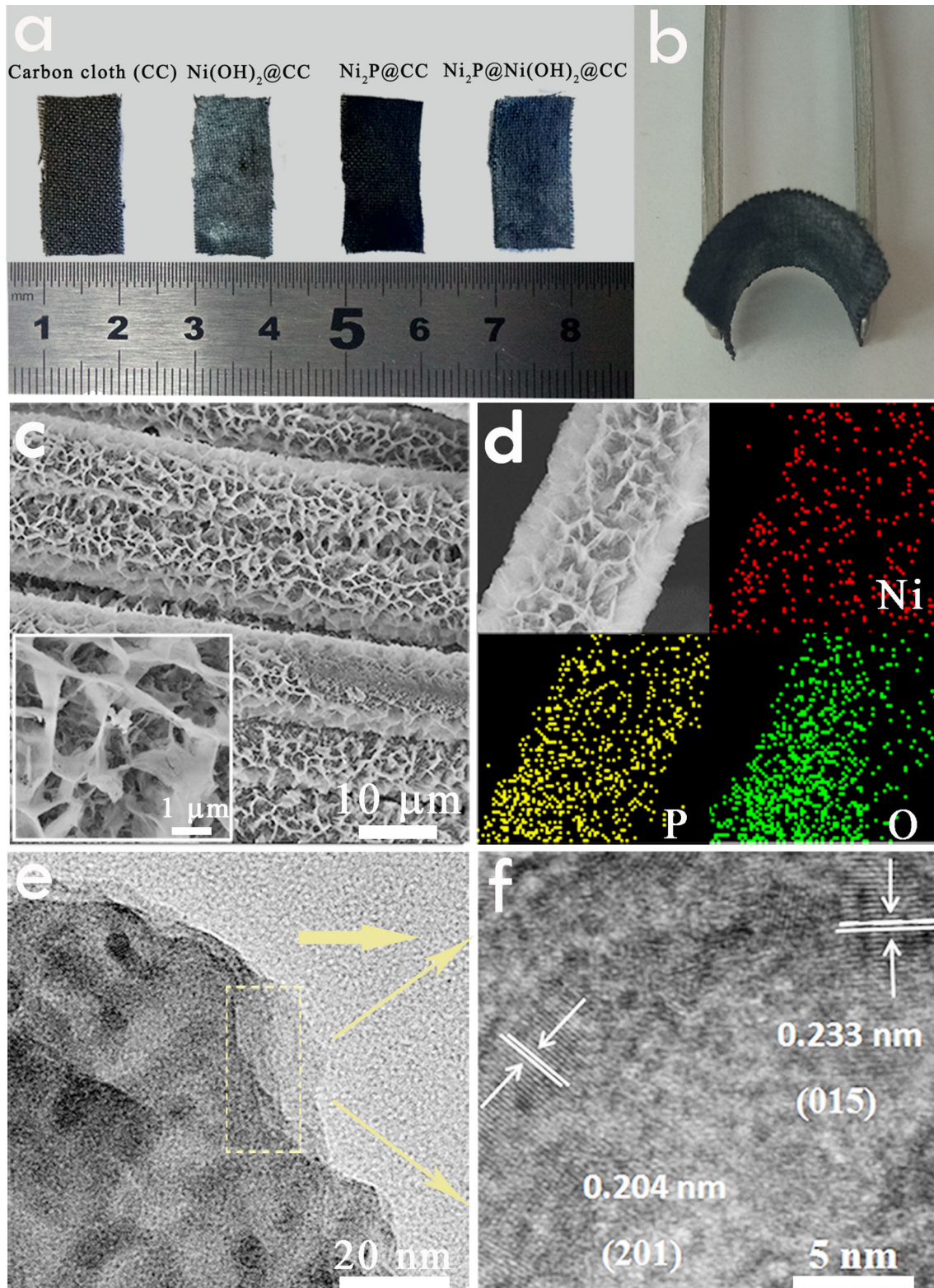


Fig. 2 **a** Optical photographs of CC substrate, $\text{Ni}(\text{OH})_2/\text{CC}$, $\text{Ni}_2\text{P}/\text{CC}$, and $\text{Ni}_2\text{P}/\text{Ni}(\text{OH})_2/\text{CC}$. **b** Optical photograph shows the flexibility of $\text{Ni}_2\text{P}/\text{Ni}(\text{OH})_2/\text{CC}$ electrode. **c** Representative SEM images of $\text{Ni}_2\text{P}/\text{Ni}(\text{OH})_2/\text{CC}$. Inset

shows the magnifying image of $\text{Ni}_2\text{P}/\text{Ni}(\text{OH})_2$ nanosheet arrays on CC substrate. **d** EDS elemental mappings of Ni, P, and O in $\text{Ni}_2\text{P}/\text{Ni}(\text{OH})_2/\text{CC}$. **e** TEM and **f** HRTEM images of $\text{Ni}_2\text{P}/\text{Ni}(\text{OH})_2$ nanosheets scraped off from the CC substrate

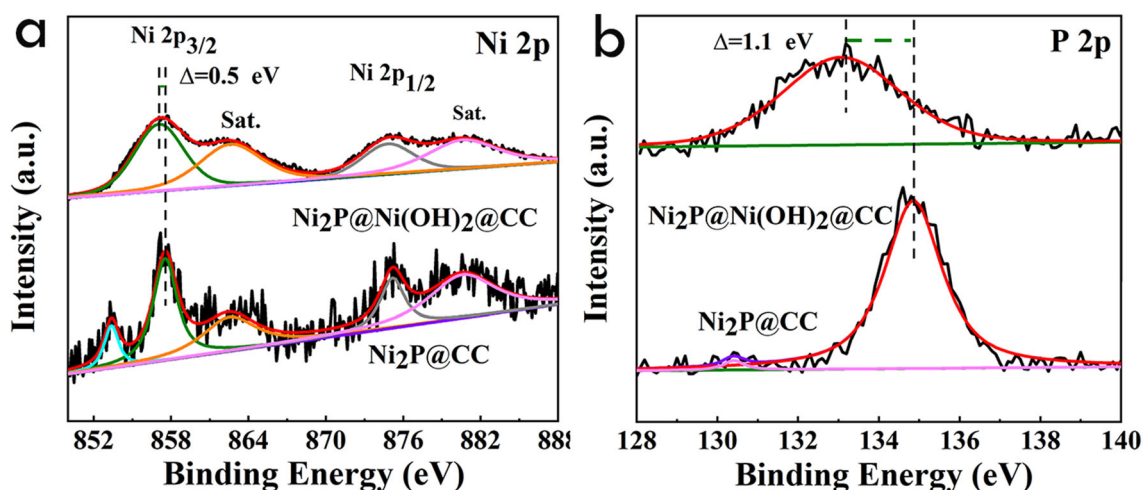


Fig. 3 XPS spectra of **a** Ni 2p and **b** P 2p for Ni₂P@CC and Ni₂P@Ni(OH)₂@CC

strong electronic interaction can generate internal electric fields, resulting in the improvement of electronic conductivity at the interfaces [34]. These results suggest that the in situ growth of Ni(OH)₂ may greatly affect the electrochemical performance of Ni₂P.

Figure 4a shows the CV curves of Ni₂P@CC and Ni₂P@Ni(OH)₂@CC electrodes at a sweep rate of 5 mV s⁻¹. Figure 4b reveals the GCD curves of the two electrodes measured at a current density of 1 mA cm⁻². The CV and GCD measurements for the two electrodes are carried out within a potential window from -0.2 to 0.6 V. Both the Ni₂P@CC and Ni₂P@Ni(OH)₂@CC electrodes exhibit broad redox reaction peaks with noticeable faradaic current (Fig. 4a) and clearly potential platform (Fig. 4b), indicating a representative battery-type pseudocapacitive feature [41, 46]. Obviously, the covering area of CV curve and discharge time of GCD curve of the Ni₂P@Ni(OH)₂@CC electrode are far higher than those of Ni₂P@CC electrode, which directly indicates that the second growth of Ni(OH)₂ can greatly increase the specific capacitance and electrochemical performance of Ni₂P. Figure 4c shows the typical CV curves of Ni₂P@Ni(OH)₂@CC electrode measured at different sweep rates ranging from 5 to 50 mV s⁻¹. Two distinct redox peaks can be observed, which are related to the reversible electrochemical reactions of Ni²⁺ in the electrolyte. By increasing the scanning rates from 5 to 50 mV s⁻¹, the redox current increases gradually and the redox peaks shift to lower potential, which are mainly attributed to the charge diffusion polarization during the charging process [47, 48].

Figure 4d reveals the GCD curves of Ni₂P@Ni(OH)₂@CC electrode measured at various current densities ranging from 1 to 10 mA cm⁻². All the GCD curves present clearly potential platform, which further indicates the outstanding battery-type pseudocapacitive characteristics. Compared with Ni₂P@CC (Fig. S5), the GCD curves of Ni₂P@Ni(OH)₂@CC electrode at different current densities show more symmetric potential-time shape, suggesting that the Ni₂P@Ni(OH)₂@CC electrode shows higher charge/discharge coulombic efficiency with lower electric polarization. Figure 4e shows the comparison of areal capacitances and gravimetric capacitances between Ni₂P@CC and Ni₂P@Ni(OH)₂@CC electrodes at various current densities, which were calculated from the GCD curves according to the Eqs. (1) and (2). Noteworthy, compared to Ni₂P@CC, the Ni₂P@Ni(OH)₂@CC electrode has higher areal capacitances and gravimetric capacitances in the whole current densities. At a low current density of 1 mA cm⁻², the Ni₂P@Ni(OH)₂@CC electrode has a gravimetric capacitance of 632 C g⁻¹ and areal capacitance of 0.73 C cm⁻², which are 2 and 2.7 times larger than those of Ni₂P@CC (321 C g⁻¹ and 0.27 C cm⁻²), respectively. At a high current density of 10 mA cm⁻², the gravimetric capacitances of Ni₂P@Ni(OH)₂@CC and Ni₂P@CC electrodes are 400 and 138 C g⁻¹, respectively. The Ni₂P@Ni(OH)₂@CC electrode has an improved rate capability of 63.3%, while the rate capability of Ni₂P@CC is only 42.9%.

Electrochemical impedance spectra (EIS) is used to evaluate the ions migration rate on the surface of

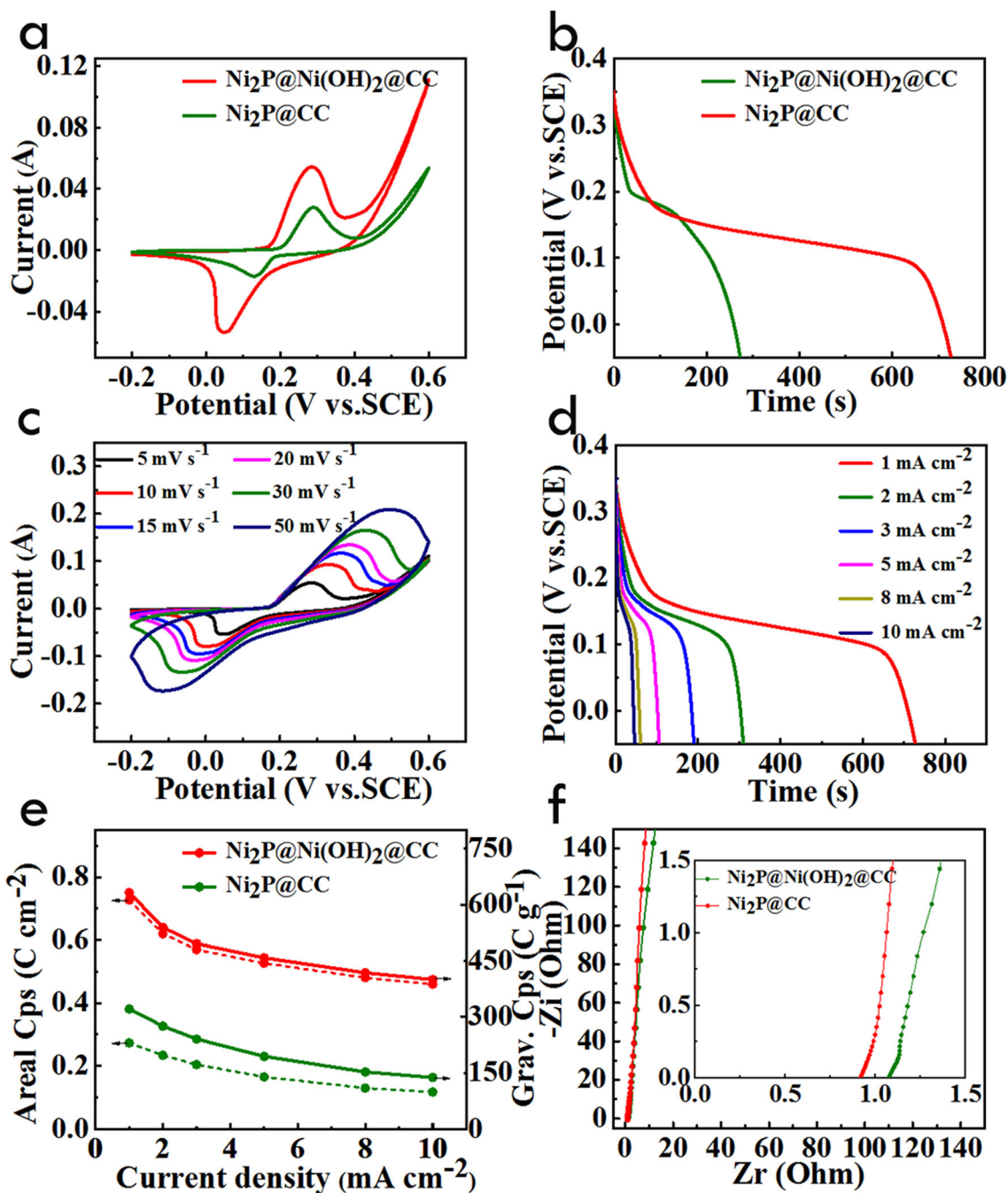


Fig. 4 a CV curves of Ni₂P@CC and Ni₂P@Ni(OH)₂@CC electrodes at 5 mV s⁻¹. b GCD curves of Ni₂P@CC and Ni₂P@Ni(OH)₂@CC electrodes at 1 mA cm⁻². c CV curves of Ni₂P@Ni(OH)₂@CC electrode at different scan rates. d GCD curves of Ni₂P@Ni(OH)₂@CC electrodes at different current

densities. e Areal capacitances and gravimetric capacitances of Ni₂P@CC and Ni₂P@Ni(OH)₂@CC electrodes at various current densities. f EIS of Ni₂P@CC and Ni₂P@Ni(OH)₂@CC electrodes. Inset is a view of the high-frequency region

electrodes, and the transport kinetics of charge diffusion, which is carried out at an open-circuit potential in the frequency ranging from 0.01 Hz to 100 kHz. Figure 4f shows the Nyquist impedance plot of Ni₂P@CC and Ni₂P@Ni(OH)₂@CC electrodes.

The real-axis intercept at the high frequency range represents ohmic series impedance (R_s), which reflects the ionic resistance of electrolyte, inherent resistances of electrodes, and interface resistance [49]. And we also use the R_s to reflect the conductivity of

the materials [50, 51]. R_s of $\text{Ni}_2\text{P@Ni(OH)}_2\text{@CC}$ electrode (0.9168Ω) was decreased in comparison with that of $\text{Ni}_2\text{P@CC}$ (1.077Ω). This suggests that $\text{Ni}_2\text{P@Ni(OH)}_2\text{@CC}$ has better electron conductivity and excellent pathways for electron transport [45], which is desirable for high power density. The result is accordant with the CV and GCD results, which indicates that $\text{Ni}_2\text{P@Ni(OH)}_2\text{@CC}$ has much better electrochemical performance than $\text{Ni}_2\text{P@CC}$.

In order to investigate the charge storage mechanism of $\text{Ni}_2\text{P@CC}$ and $\text{Ni}_2\text{P@Ni(OH)}_2\text{@CC}$ electrodes, the corresponding CV results were further analyzed (Figs. S6 and 4c). Generally, the relationship between measured current (i) and scan rate (v) obeys the power law [52–55]:

$$i = av^b, \tag{7}$$

where both a and b are constants. In the case of diffusion-controlled and surface capacitive processes, b value approaches 0.5 and 1, respectively. Figure 5 shows the fitting results of b value using anodic peaks. The b values of $\text{Ni}_2\text{P@CC}$ and $\text{Ni}_2\text{P@Ni(OH)}_2\text{@CC}$ are calculated to be 0.50 and 0.62, respectively. This result suggests that diffusion process is the major factors that determine the electrochemical properties of Ni_2P and $\text{Ni}_2\text{P@Ni(OH)}_2$. Compared to Ni_2P , the introduction of Ni(OH)_2 can improve the surface capacitive ability of $\text{Ni}_2\text{P@Ni(OH)}_2$.

Cycling stability is another important criterion in the supercapacitor applications, as shown in Fig. 6.

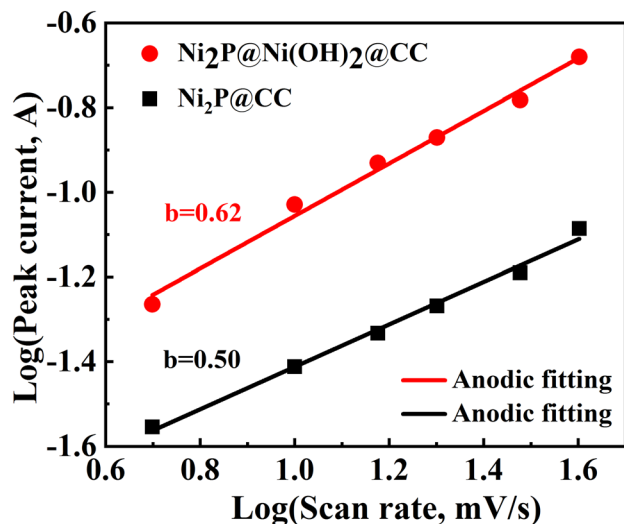


Fig. 5 Relationship between logarithm anodic peak currents and logarithm scan rates

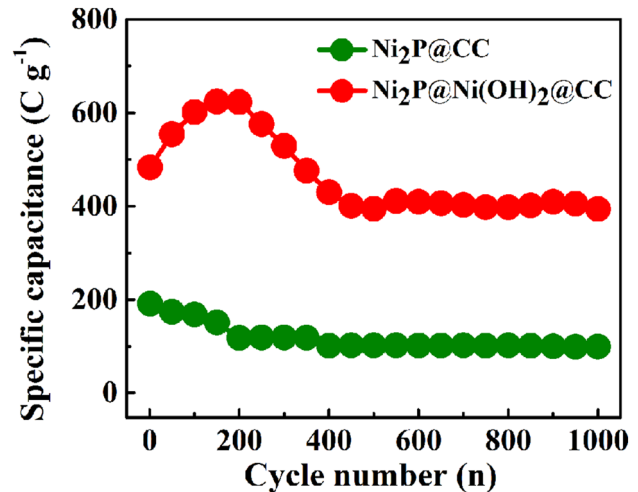


Fig. 6 Cycling stabilities of $\text{Ni}_2\text{P@CC}$ and $\text{Ni}_2\text{P@Ni(OH)}_2\text{@CC}$ at a current density of 2 mA cm^{-2}

The capacitive retention of $\text{Ni}_2\text{P@Ni(OH)}_2\text{@CC}$ electrode was approximately 81.4% after 1000 charge/discharge cycles at a constant current density of 2 mA cm^{-2} , much higher than that of $\text{Ni}_2\text{P@CC}$ (51.8%). Compared to $\text{Ni}_2\text{P@CC}$ electrode, the capacitive retention of the $\text{Ni}_2\text{P@Ni(OH)}_2\text{@CC}$ electrode increases in the early cycles and keeps unchanged, indicating that this electrode material has a good cycling stability. The initial increase in specific capacity could be ascribed to the infiltration and activation of $\text{Ni}_2\text{P@Ni(OH)}_2\text{@CC}$ electrode, which is also present in other phosphide materials [56]. Besides, the $\text{Ni}_2\text{P@Ni(OH)}_2\text{@CC}$ electrode exhibits over 95% of coulombic efficiency after 1000 charge-discharge cycles, demonstrating good stability (Fig. S7). And the SEM image of $\text{Ni}_2\text{P@Ni(OH)}_2\text{@CC}$ electrode after electrochemical testing is shown in Fig. S8. Its morphology can still maintain the multi-stage nanosheets structure, indicating that the electrode material has good structural stability. The good cycling stability is mainly due to the unique three-dimensional hierarchical architecture with self-assembled uninterrupted ultrathin nanosheets on the surface of the material.

To further investigate the potential applications of the electrode, a hybrid supercapacitors (HSC) device was assembled by employing $\text{Ni}_2\text{P@Ni(OH)}_2\text{@CC}$ as the anode and AC as the cathode. To satisfy the charge balance, the mass of AC was calculated using the Eqs. (3) and (4). Figure 7a reveals the CV curves of the HSC device measured at different scan rates, which show a potential window of 0–1.6 V. GCD

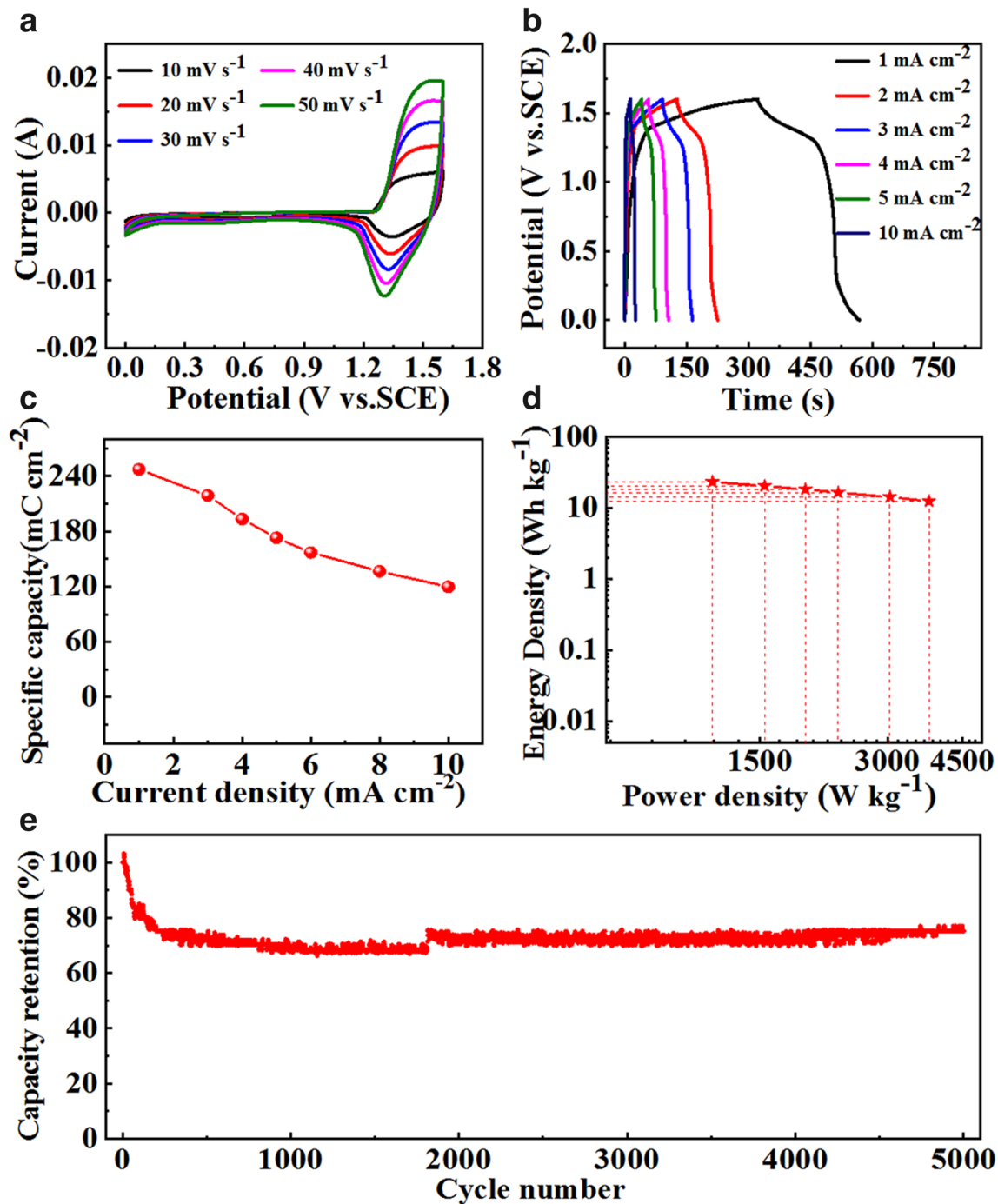


Fig. 7 $\text{Ni}_2\text{P}@\text{Ni}(\text{OH})_2@\text{CC}//\text{AC}$ hybrid supercapacitors: **a** CV curves at different scan rates. **b** GCD curves at different current densities. **c** The specific capacitances at different current densities.

curves of the HSC device are displayed in Fig. 7b. A clear potential platform can be seen in all the GCD curves measured at different current densities, suggesting that the device should possess both electrical double-layer capacity and battery-like capacity.

d Ragone plots of power density and energy density. **e** Cycling stability at 5 mA cm^{-2} for 5000 cycles

Figure 7c shows the corresponding specific capacitances obtained from Fig. 7b. The specific capacitances are 247.4 and 119.8 mC cm^{-2} at 1 and 10 mA cm^{-2} , respectively. The energy density and power density of the $\text{Ni}_2\text{P}@\text{Ni}(\text{OH})_2@\text{CC}//\text{AC}$ HSC

device were calculated by Eqs. (5) and (6). Figure 7d shows the Ragone plots of energy densities and power densities obtained from the GCD curves. The maximum energy density reaches 23.5 Wh kg^{-1} at a power density of 1158.0 W kg^{-1} , and remains 12.5 Wh kg^{-1} at 3756.3 W kg^{-1} . Table S2 shows the comparison of energy densities and power densities of $\text{Ni}_2\text{P@Ni(OH)}_2\text{/CC//AC}$ device with other Ni-based phosphides HSC devices. Obviously, the $\text{Ni}_2\text{P@Ni(OH)}_2\text{/CC//AC}$ device represents comparable or even better energy densities. Figure 7e displays the cycling stability performance of $\text{Ni}_2\text{P@Ni(OH)}_2\text{/CC//AC}$ HSC device. The charge/discharge cycles were operated at 5 mA cm^{-2} for 5000 cycles. The $\text{Ni}_2\text{P@Ni(OH)}_2\text{/CC//AC}$ HSC device reveals good cycling stability, which possesses 75.2% maintenance after 5000 cycles.

4 Conclusion

In summary, three-dimensional hierarchical $\text{Ni}_2\text{P@Ni(OH)}_2$ architecture was in situ grown on a flexible carbon cloth substrate, which was used as a novel binder-free hybrid-type electrode for supercapacitor applications. Taking the combined benefits of high electronic conductivity of N_2P , superior anion exchanging/intercalating capacity of Ni(OH)_2 , special 3D porous hierarchical architectures, and excellent flexibility of carbon cloth, the $\text{Ni}_2\text{P@Ni(OH)}_2\text{/CC}$ electrode shows boosting specific capacitance, rate capability, and charge/discharge cycle stability in comparison with $\text{Ni}_2\text{P/CC}$. Charge storage mechanism investigations show that the introduction of Ni(OH)_2 can improve the surface capacitive ability of Ni_2P . The assembly $\text{Ni}_2\text{P@Ni(OH)}_2\text{/CC//AC}$ hybrid supercapacitor device shows high energy density and good cycling stability. This study demonstrates that the three-dimensional hierarchical $\text{Ni}_2\text{P@Ni(OH)}_2\text{/CC}$ architecture with advanced synergistic effects holds great promise as hybrid electrode for supercapacitors.

Acknowledgements

This work was supported by the National Natural Science Foundation of China (51572218), Natural Science Foundation of Shaanxi Province (2017KCT-01, 2019JM-138), Scientific Research Program Funded

by Shaanxi Provincial Education Department (18JK0786), Young Talent Fund of University Association for Science and Technology in Shaanxi (20170605), and Key Project of Research and Development of Shaanxi Province (2018ZDCXL-GY-08-05).

Compliance with ethical standards

Conflict of interest The authors declare no conflicts of interest.

Supplementary Information: The online version contains supplementary material available at <http://doi.org/10.1007/s10854-021-05521-5>.

References

1. J.T. Zhang, X.S. Zhao, On the configuration of supercapacitors for maximizing electrochemical performance. *ChemSuschem* **5**, 818–841 (2012)
2. X.R. Li, J.L. Wei, Q. Li, S.S. Zheng, Y.X. Xu, P. Du, C.Y. Chen, J.J. Zhao, H.G. Xue, Q. Xu, H. Pang, Nitrogen-doped cobalt oxide nanostructures derived from cobalt-alanine complexes for high-performance oxygen evolution reactions. *Adv. Funct. Mater.* **28**, 1800886 (2018)
3. Y.H. Feng, S.H. Chen, J. Wang, B.A. Lu, Carbon foam with microporous structure for high performance symmetric potassium dual-ion capacitor. *J. Energy Chem.* **43**, 129–138 (2020)
4. X.R. Li, X.C. Yang, H.G. Xue, H. Pang, Q. Xu, Metal-organic frameworks as a platform for clean energy applications. *EnergyChem.* **2**, 100027 (2020)
5. X.Z. Yu, B.A. Lu, Z. Xu, Super long-life supercapacitors based on the construction of nanohoneycomb-like strongly coupled $\text{CoMoO}_4\text{-3D}$ graphene hybrid electrodes. *Adv. Mater.* **26**, 1044–1051 (2014)
6. P. Poizot, F. Dolhem, Clean energy new deal for a sustainable world: from non- CO_2 generating energy sources to greener electrochemical storage devices. *Energy Environ. Sci.* **4**, 2003 (2011)
7. B.W. He, P.Y. Kuang, X.H. Li, H. Chen, J.G. Yu, K. Fan, In situ transformation of Prussian-blue analogue-derived bimetallic carbide nanocubes by water oxidation: applications for energy storage and conversion. *Chem. Eur. J.* **25**, 1–12 (2019)
8. G.P. Wang, L. Zhang, J.J. Zhang, A review of electrode materials for electrochemical supercapacitors. *Chem. Soc. Rev.* **41**, 797–828 (2012)
9. C. Peng, S.W. Zhang, X.H. Zhou, G.Z. Chen, Unequalisation of electrode capacitances for enhanced energy capacity in

- asymmetrical supercapacitors. *Energy Environ. Sci.* **3**, 1499–1502 (2010)
10. G.Q. Zhang, H.B. Wu, H.E. Hoster, M.B. Chan-Park, X.W. (David) Lou, Single-crystalline NiCo₂O₄ nanoneedle arrays grown on conductive substrates as binder-free electrodes for high-performance supercapacitors. *Energy Environ. Sci.* **5**, 9453–9456 (2012)
 11. J.R. Miller, P. Simon, Electrochemical capacitors for energy management. *Science* **321**, 651–652 (2008)
 12. W. Zhou, K. Yu, D. Wang, J. Chu, J. Li, L. Zhao, C. Ding, Y. Du, X. Jia, H. Wang, G. Wen, Hierarchically constructed NiCo₂S₄@Ni_(1-x)Co_x(OH)₂ core/shell nanoarrays and their application in energy storage. *Nanotechnology* **27**, 235402 (2016)
 13. S. Peng, L. Li, H.B. Wu, S. Madhavi, X.W. (David) Lou, Controlled growth of NiMoO₄ nanosheet and nanorod arrays on various conductive substrates as advanced electrodes for asymmetric supercapacitors. *Adv. Energy Mater.* **5**, 1401172 (2015)
 14. T. Liu, L.Y. Zhang, W. You, J.G. Yu, Core-shell nitrogen-doped carbon hollow spheres/Co₃O₄ nanosheets as advanced electrode for high-performance supercapacitor. *Small* **14**, 1702407 (2018)
 15. Y. Zhong, X. Xia, F. Shi, J. Zhan, J. Tu, H.J. Fan, Transition metal carbides and nitrides in energy storage and conversion. *Adv. Sci.* **3**, 1500286 (2016)
 16. E. Frackowiak, Carbon materials for supercapacitor application. *Phys. Chem. Chem. Phys.* **9**, 1774–1785 (2007)
 17. Y. Wang, Y. Xia, Recent progress in supercapacitors: from materials design to system construction. *Adv. Mater.* **25**, 5336–5342 (2013)
 18. P. Simon, Y. Gogotsi, Materials for electrochemical capacitors. *Nat. Mater.* **7**, 845–854 (2008)
 19. Y.Z. Hu, C.H. Huang, S.P. Jiang, Y.L. Qin, H. Chen, Hierarchical nickel-cobalt selenide nanoparticles/nanosheets as advanced electroactive battery materials for hybrid supercapacitors. *J. Colloid Interface Sci.* **558**, 291–300 (2020)
 20. W.L. Hong, L.Y. Lin, Design of nickel cobalt oxide and nickel cobalt oxide@nickel molybdenum oxide battery-type materials for flexible solid-state battery supercapacitor hybrids. *J. Power Sources* **435**, 226797 (2019)
 21. Y.M. Hu, M.C. Liu, Y.X. Hu, Q.Q. Yang, L.B. Kong, L. Kang, One-pot hydrothermal synthesis of porous nickel cobalt phosphides with high conductivity for advanced energy conversion and storage. *Electrochim. Acta* **215**, 114–125 (2016)
 22. J. Wen, S.Z. Li, T. Chen, B. Li, L.B. Xiong, Y.X. Guo, G.J. Fang, Porous nanosheet network architecture of CoP@Ni(OH)₂ composites for high performance supercapacitors. *Electrochim. Acta* **258**, 266–273 (2017)
 23. X. Li, H. Wu, A.M. Elshahawy, L. Wang, S.J. Pennycook, C. Guan, J. Wang, Cactus-like NiCoP/NiCo-OH 3D architecture with tunable composition for high-performance electrochemical capacitors. *Adv. Funct. Mater.* **28**, 1800036 (2018)
 24. S. Wang, Z. Xiao, S. Zhai, G. Wang, Q. An, D. Yang, A high-temperature phosphorization for synthesis of core-shell Ni_xP_y@C nanocomposite-immobilized sponge-like P-doped porous carbon with excellent supercapacitance performance. *Electrochim. Acta* **309**, 197–208 (2019)
 25. Y. Xu, S. Hou, G. Yang, X. Wang, T. Lu, L. Pan, Synthesis of bimetallic Ni_xCo_{1-x}P hollow nanocages from metal-organic frameworks for high performance hybrid supercapacitors. *Electrochim. Acta* **285**, 192–201 (2018)
 26. X. Li, A. MEIshahawy, C. Guan, J. Wang, Metal phosphides and phosphates-based electrodes for electrochemical supercapacitors. *Small* **13**, 1701530 (2017)
 27. D. Wang, L.B. Kong, M.C. Liu, W.B. Zhang, Y.C. Luo, L. Kang, Amorphous Ni-P materials for high performance pseudocapacitors. *J. Power Sources* **274**, 1107–1113 (2015)
 28. H. Wu, Y.H. Ni, M.F. Wang, D.C. Lu, Shape-controlled synthesis and performance comparison of Ni₂P nanostructures. *CrystEngComm* **18**, 5155–5163 (2016)
 29. J.L. Xing, J. Du, X. Zhang, Y.B. Shao, T. Zhang, C.L. Xu, A Ni-P@NiCo LDH core-shell nanorod-decorated nickel foam with enhanced areal specific capacitance for high-performance supercapacitors. *Dalton Trans.* **46**, 10064 (2017)
 30. Y. Cheng, Y.F. Zhang, H.M. Jiang, X.Y. Dong, J.Q. Zheng, C.G. Meng, Synthesis of amorphous cobalt silicate nanobelts@manganese silicate core-shell structures as enhanced electrode for high-performance hybrid supercapacitors. *J. Colloid Interface Sci.* **561**, 762–771 (2020)
 31. M. Racik, A. Manikandan, M. Mahendiran, J. Madhavana, M.V. Antony Raj, M.G. Mohamed, T. Maiyalagan, Hydrothermal synthesis and characterization studies of α-Fe₂O₃/MnO₂ nanocomposites for energy storage supercapacitor application. *Ceram. Int.* **46**, 6222–6233 (2020)
 32. Y.H. Tian, L.Y. Lin, M.L. Ning, S. Hussain, H. Su, M.S. Javed, H.J. Zhen, N. Hu, A. Shaheen, Novel binder-free electrode of NiCo₂O₄@NiMn₂O₄ core-shell arrays modified carbon fabric for enhanced electrochemical properties. *Ceram. Int.* **45**, 16904–16910 (2019)
 33. T.F. Yi, J. Mei, B.L. Guan, P. Cui, S.H. Luo, Y. Xie, Y.G. Liu, Construction of spherical NiO@MnO₂ with core-shell structure obtained by depositing MnO₂ nanoparticles on NiO nanosheets for high-performance supercapacitor. *Ceram. Int.* **46**, 421–429 (2020)
 34. X. Gao, Y. Zhao, K. Dai, J. Wang, B. Zhang, X. Shen, NiCoP nanowire@NiCo-layered double hydroxides nanosheet heterostructure for flexible asymmetric supercapacitors. *Chem. Eng. J.* **384**, 123373 (2020)

35. Z. Ma, F. Jing, Y. Fan, L. Hou, L. Su, L. Fan, G. Shao, High-stability MnO_x nanowires@C@ MnO_x nanosheet core-shell heterostructure pseudocapacitance electrode based on reversible phase transition mechanism. *Small* **15**, 1900862 (2019)
36. J. Yang, C. Yu, X. Fan, J. Qiu, 3D Architecture materials made of NiCoAl-LDH nanoplates coupled with NiCo-carbonate hydroxide nanowires grown on flexible graphite paper for asymmetric supercapacitors. *Adv. Energy Mater.* **4**, 1400761–1400769 (2014)
37. Z. Lu, W. Zhu, X. Lei, G.R. Williams, D. O'Hare, Z. Chang, X. Sun, X. Duan, High pseudocapacitive cobalt carbonate hydroxide films derived from CoAl layered double hydroxides. *Nanoscale* **4**, 3640–3643 (2012)
38. S.C. Sekhar, G. Nagaraju, J.S. Yu, Conductive silver nanowires-fenced carbon cloth fibers-supported layered double hydroxide nanosheets as a flexible and binder-free electrode for high-performance asymmetric supercapacitors. *Nano Energy* **36**, 58–67 (2017)
39. D.D. Wei, Y.L. Zhang, X.Z. Zhu, M.L. Fan, Y.L. Wang, CNT/ Co_3S_4 @NiCo LDH ternary nanocomposites as battery-type electrode materials for hybrid supercapacitors. *J. Alloys Compd.* **824**, 153937 (2019)
40. J. Wang, Q. Zhong, Y.Q. Zeng, D.Y. Cheng, Y.G. Xiong, Y.F. Bu, Rational construction of triangle-like nickel-cobalt bimetallic metal-organic framework nanosheets arrays as battery-type electrodes for hybrid supercapacitors. *J. Colloid Interface Sci.* **555**, 42–52 (2019)
41. H.C. Chen, S.P. Jiang, B.H. Xu, C.H. Huang, Y.Z. Hu, Y.L. Qin, M.X. He, H.J. Cao, Sea-urchin-like nickel-cobalt phosphide/phosphate composites as advanced battery materials for hybrid supercapacitors. *J. Mater. Chem. A* **7**, 6241 (2019)
42. C.X. Zhou, T.T. Gao, Y.J. Wang, Q.L. Liu, D. Xiao, Through a hydrothermal phosphatization method synthesized NiCo and Fe based electrodes for high-performance battery-supercapacitor hybrid device. *Appl. Surf. Sci.* **475**, 729–739 (2019)
43. B.B. Cheng, W. Zhang, M. Yang, Y.J. Zhang, F.B. Meng, Preparation and study of porous MnCo_2O_4 @NiO nanosheets for high-performance supercapacitor. *Ceram. Int.* **45**, 20451–20457 (2019)
44. X.J. Zhang, S.J. Hou, Z.B. Ding, G. Zhu, H.R. Tang, Y.C. Hou, T. Lu, L.K. Pan, Carbon wrapped CoP hollow spheres for high performance hybrid supercapacitor. *J. Alloys Compd.* **822**, 153578 (2019)
45. H.J. Zhang, X.P. Li, A. Hähnel, V. Naumann, C. Lin, S. Azimi, S.L. Schweizer, A.W. Maijenburg, R.B. Wehrspohn, Bifunctional heterostructure assembly of NiFe LDH nanosheets on NiCoP nanowires for highly efficient and stable overall water splitting. *Adv. Funct. Mater.* **28**, 1706847 (2018)
46. Q. Zong, H. Yang, Q.Q. Wang, Q.L. Zhang, Y.L. Zhu, H.Y. Wang, Q.H. Shen, Three-dimensional coral-like NiCoP@C@Ni(OH)₂ core-shell nanoarrays as battery-type electrodes to enhance cycle stability and energy density for hybrid supercapacitors. *Chem. Eng. J.* **361**, 1–11 (2019)
47. D. Wang, L.B. Kong, M.C. Liu, Y.C. Luo, L. Kang, An approach to preparing Ni-P with different phases for use as supercapacitor electrode materials. *Chem. Eur. J.* **21**, 17897–17903 (2015)
48. X.D. Li, R. Ding, W. Shi, Q.L. Xu, L. Wang, H.X. Jiang, Z. Yang, E.H. Liu, Hierarchical mesoporous Ni-P@ MnO_2 composite for high performance supercapacitors. *Mater. Lett.* **187**, 144–147 (2017)
49. Z. Hu, Z.M. Liu, J.G. Zhao, X.Z. Yu, B.A. Lu, Rose-petals-derived hemispherical micropapillae carbon with cuticular folds for super potassium storage. *Electrochim. Acta* **368**, 137629 (2021)
50. S.S. Zheng, Q. Li, H.G. Xue, H. Pang, Q. Xu, A highly alkaline-stable metal oxide@metal-organic framework composite for high-performance electrochemical energy storage. *Natl. Sci. Rev.* **7**, 305–314 (2020)
51. S.S. Zheng, X.T. Guo, H.G. Xue, K.M. Pan, C.S. Liu, H. Pang, Facile one-pot generation of metal oxide/hydroxide@metal organic framework composites: highly efficient bifunctional electrocatalysts for overall water splitting. *ChemComm* **55**, 10904–10907 (2019)
52. X. Wang, Y. Fang, B. Shi, F. Huang, F. Rong, R. Que, Three-dimensional NiCo_2O_4 @ NiCo_2O_4 core-shell nanocones arrays for high-performance supercapacitors. *Chem. Eng. J.* **344**, 311–319 (2018)
53. Y.Y. Lan, H.Y. Zhao, Y. Zong, X.H. Li, Y. Sun, J. Feng, Y. Wang, X.L. Zheng, Y.P. Du, Phosphorization boosts the capacitance of mixed metal nanosheet arrays for high performance supercapacitor electrodes. *Nanoscale* **10**, 11775–11781 (2018)
54. N. Feng, R.J. Meng, L.H. Zu, Y.T. Feng, C.X. Peng, J.M. Huang, G.L. Liu, B.J. Chen, J.H. Yang, A polymer-direct-intercalation strategy for MoS_2 /carbon-derived heteroerogels with ultrahigh pseudocapacitance. *Nat. Commun.* **10**, 1372 (2019)
55. H.B. Ding, J. Zhou, A.M. Rao, B.A. Lu, Cell-like-carbon-micro-spheres for robust potassium anode. *Natl. Sci. Rev.* (2020). <https://doi.org/10.1093/nsr/nwaa276>
56. K. Zhou, W.J. Zhou, L.J. Yang, J. Lu, S. Cheng, W.J. Mai, Z.H. Tang, L.G. Li, S.W. Chen, Ultrahigh-performance pseudocapacitor electrodes based on transition metal phosphide nanosheets array via phosphorization: a general and effective approach. *Adv. Funct. Mater.* **25**, 7530–7538 (2015)

Publisher's Note Springer Nature remains neutral with regard to jurisdictional claims in published maps and institutional affiliations.